5.3

TURBULENCE AND GRAVITY WAVES IN A DYNAMICALLY UNBALANCED UPPER-LEVEL JET-FRONTAL SYSTEM

Steven E. Koch[1] and Chungu Lu[1,2]

[1] *NOAA Earth System Research Laboratory (ESRL), Boulder, CO*
[2] *Cooperative Institute for Research in the Atmosphere (CIRA), Colorado State University, Ft. Collins, CO*

1. INTRODUCTION

The relationship between turbulence and gravity waves in upper-level jet/frontal systems is investigated using high-resolution aircraft in situ and dropsonde measurements and simulations from hydrostatic and non-hydrostatic numerical models initialized with real data. Previous studies using aircraft measurements have revealed gravity waves with scales of 2–40 km transverse to the flow at jet stream levels coexisting with turbulence (Shapiro 1978; Gultepe and Starr 1995; Demoz et al. 1998). It is unclear why such waves with scales considerably longer than those associated with clear-air turbulence (CAT) should be associated with CAT. An untested hypothesis is that since nonlinearity leads to shortening of the horizontal wavelength, eventual wave breaking, and concomitant generation of Turbulent Kinetic Energy (TKE), then turbulence may occur as the wave fronts become steeper and break due to nonlinear advection of the dominant wave in a wave packet (Hines 1963; Hodges 1967; Weinstock 1986; Cot and Barat 1986; Lindzen 1987).

Recent research indicates that gravity waves with horizontal wavelengths larger than a few kilometers may also play an important role in creating conditions conducive to Kelvin-Helmholtz instability. Significant turbulence occurs in association with gravity wave activity immediately downstream of regions of diagnosed flow imbalance at jet stream levels (Koch and Caracena 2002; Koch et al. 2005). Imbalance in these studies was defined as a large residual in the sum of the terms in the nonlinear balance equation computed from mesoscale model fields.

Spontaneous gravity wave emission forced by flow imbalance near upper-level jet/frontal systems was shown in the two-dimensional idealized modeling study of Reeder and Griffiths (1996). Idealized, three-dimensional simulations by Zhang (2004) indicate that mesoscale gravity waves are generated where such imbalance was diagnosed in preferred locations relative to a developing baroclinic system. The most pronounced of the wave modes consisted of a packet of waves transverse to the flow that forms as a diffluent jet streak approached the axis of inflection downstream of the upper-level trough, in accordance with the Uccellini and Koch (1987) conceptual model. Also, low-level gravity waves formed parallel to the surface cold front. Finally, waves were generated with wavefronts roughly parallel to the northwesterly flow upstream of the upper-level trough axis during the later stages of baroclinic development. This latter mode is investigated in detail with the observations and numerical model simulations in the current study.

This paper summarizes important results from a multiple part study of a turbulence event above the core of a very strong jet streak that occurred over the North Pacific on 17–18 February 2001. The interested reader is directed to Koch et al. (2005), Lu et al. (2005a,b), and Lane et al. (2004) for additional details. The principal measurements in this study consisted of high-resolution in-situ data and GPS dropwindsondes released at ~40-km spacing from the NOAA Gulfstream-IV (G-IV) research aircraft as it flew along a line nearly perpendicular to the upper-level winds. The G-IV aircraft documented the structure of the jet streak and wind shear patterns, the upper-level front and stable quasi-isentropic lamina, gravity waves, and the intensity of turbulence.

One of the models used in this study is the hybrid isentropic coordinate, 20-km Rapid Update Cycle (RUC) model (Benjamin et al. 2004 a, b). The isentropic framework is believed to be advantageous for the analysis of upper-level frontal systems. The RUC model domain was shifted west to the central north Pacific from its normal operational position for this study. Koch et al. (2005) provide details pertaining to the initialization and data assimilation used by the RUC. The other model used in this study is the nonhydrostatic, anelastic Clark-Hall (CH) model (Clark 1977; Clark et al. 2000), which was nested within the fully compressible, nonhydrostatic Coupled Ocean-Atmosphere Mesoscale Prediction System (COAMPS™) model of the Navy (Hodur 1997). The

Corresponding author address: *Steven E. Koch, NOAA/OAR/ESRL, R/GSD, 325 Broadway, Boulder, CO 80305-3328; e-mail <* Steven.Koch@noaa.gov*>*

highest resolution nest of the CH model was a 1-km grid offering 50-m vertical resolution and a Rayleigh friction absorber to reduce gravity wave reflections from the upper boundary, which was placed at 30 km. Lane et al. (2004) provide additional details about the CH and COAMPS model configurations.

This paper also utilizes novel methods of analysis with the 25-Hz aircraft data to separate waves from turbulence and to examine their interactions. Since in the real world, gravity waves are often not monochromatic, and they are highly transient owing to interactions of various physical mechanisms (e.g., wave-wave and wave-turbulence interactions, wave breaking and dissipation), an analysis tool enabling us to study rapid changes in wave amplitudes and phases was found to be necessary. We developed a method for combining traditional cross-spectral and wavelet transformation to construct the time-varying spectrum of waves (Lu et al. 2005a), and then introduced this new technique into the Stokes partially polarized wave parameter technique so as to identify polarization signatures of waves distinct from those of turbulence (Lu et al. 2005b).

2. MESOSCALE ANALYSIS

The G-IV took off from Hawaii along a northward track toward a strong jet streak and associated potential vorticity (PV) maximum approximately halfway between Hawaii and the Aleutian Islands. An intense 92 m s^{-1} jet maximum was analyzed by the RUC in the vicinity of the G-IV track, with very strong cyclonic shear to its northeast. Dropsondes launched from flight level 41Kft over the black part of the aircraft track in Fig. 1 at ~40 km intervals from 2326 UTC 17Feb to 0024 UTC 18Feb were used to construct vertical cross-section analyses enabling details of the upper-level jet/front system and gravity waves to be understood. The G-IV also collected 25-Hz meteorological and aircraft vertical acceleration in-situ data from 0000 to 0024 UTC 18 Feb at 41 000 ft, and then subsequently along three other nearly parallel legs shown in Table 1. Since the true airspeed of the aircraft was 230 m s^{-1}, the spatial resolution of these data was 9 m. However, electronics noise at a frequency of 6 Hz limited the smallest effective scale in this study to ~60 m.

Table 1. In-situ data observation times and levels for the Gulfstream-IV aircraft.

Time Period of Data	Flight level		
(UTC 18 Feb 01)	(ft)	(km)	(hPa)
0000–0024	41 000	12.5	175
0030–0052	33 000	10.1	260
0101–0017	35 000	10.7	235
0122–0140	37 000	11.4	214

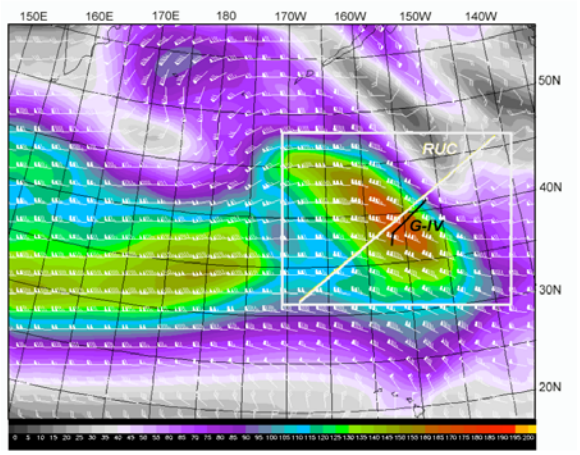

Fig. 1. Domain of the special RUC model runs showing 1-h forecast of wind barbs and isotachs at 260 hPa (33 000 ft) valid at 0100 UTC 18 February 2001 over the Pacific Ocean (note the Hawaiian and Aleutian Islands). Isotach values (kt) are shown in the color bar at the bottom of the figure (forecast maximum wind is 92 m s^{-1}). The G-IV flew from the core of a very strong jet streak to its cyclonic side. The white rectangle depicts the domain over which gravity waves were analyzed. Also depicted is the location of the model cross sections shown below (white line), and that of a smaller segment over which the Gulfstream-IV released dropsondes (black line).

Isentropic cross sections of PV from the RUC model (Fig. 2) show an intensifying upper-level front, as inferred from the increasing slope of the isentropes in the 250–350 hPa layer at $600 < x < 1400$ km. The strengthening of this front and associated jet streak (not shown) are directly linked to frontogenesis in the upper troposphere, as discussed below. Strong static stability and cyclonic shear along the bottom of the upper-level front support a pronounced tropopause fold, which descends from 550 to 650 hPa during this 6h period. Also of interest is a *secondary* tropopause fold immediately above the primary fold that increasingly stretches out with time along a stable lamina near 350 hPa. Both of these folds were apparent in the initial state of the RUC at 2100 UTC. By contrast, there are several very fine-scale features in the PV field that *developed* in the forecasts. These "tropopause undulations," which lie directly above the secondary fold (highlighted by the 325K isentrope), are actually upward-propagating gravity waves directly associated with the developing upper-level front (Koch et al. 2005). They have strong counterparts in the dropsonde data analysis and their vertical and horizontal wavelengths of 1.8 and 216 km are comparable to those seen in the CH model forecasts. The gravity waves were a robust feature of both the RUC and CH models.

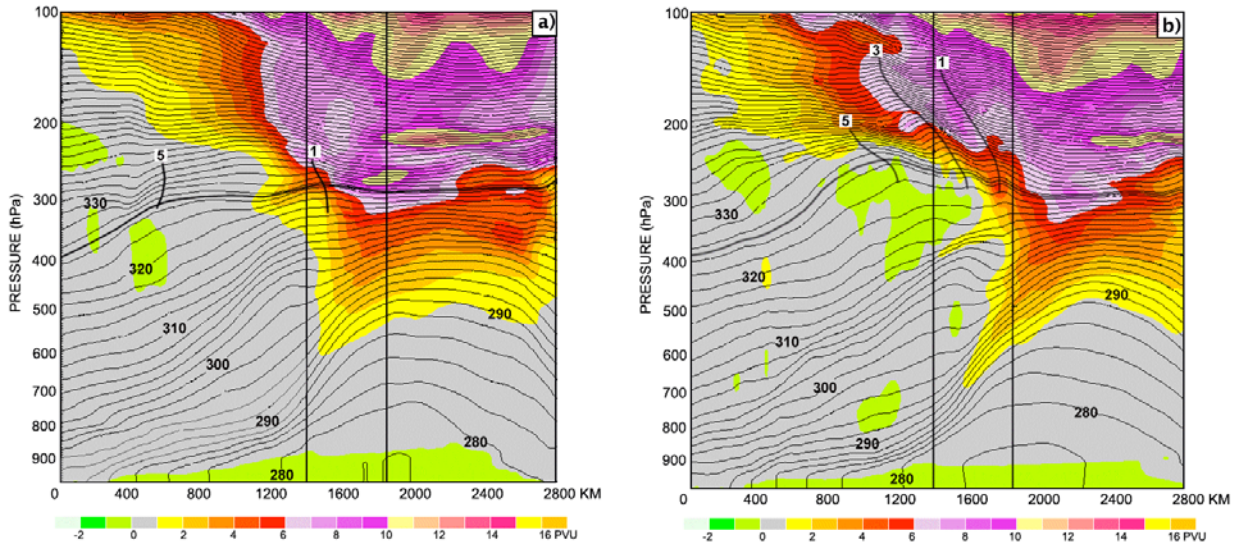

Fig. 2. RUC vertical cross sections (cf. Fig. 1) of isentropes (2K contours) and Ertel's potential vorticity (1 PVU = 1 x 10^{-6} K kg^{-1} m^2 s^{-1}, PVU values given by color shading, see color bar) along a 2800-km path perpendicular to the jet stream flow. The cross section in (a) is from the RUC analysis at 2100 UTC 17 February, whereas that in (b) is from the 6-h forecast valid at 0300 UTC 18 February. Vertical lines denote the ~400-km segment over which the G-IV took measurements. The 325-K isentrope is highlighted to emphasize the fluctuations associated with gravity waves 1, 3, and 5 (#2 and #4 appear at other times). Tropopause fold is defined by values of potential vorticity >1.5 PVU.

3. FRONTOGENESIS, GRAVITY WAVES, AND TURBULENCE INTERACTIONS

Several different measures of turbulence were computed from the G-IV data and the numerical models, including the gradient Richardson number, the DTF3 turbulence diagnostic, and TKE assuming unity for the Prandtl number (Koch et al. 2005). Diagnosed turbulence appeared in local regions of strong vertical wind shear directly above and below the jet core. The spatial structure of the turbulence fields was even more interesting. A strikingly banded nature to the DTF3 fields at 33 000 ft (10.1 km) is apparent in the RUC forecast for 0300 UTC (Fig. 3b). The bands are parallel both with the flow and with an intensifying frontal zone just to their west as seen in the packing of the isotherms at 275 hPa and the diagnosis of strong frontogenesis in a band oriented parallel to the narrower DTF3 bands (Fig. 3a). These bands in DTF3 are directly coupled to the gravity waves mentioned earlier. Similar patterns appear in the sub-grid TKE and perturbation potential temperature fields on constant-height surfaces in the 1-km resolution CH model (the model domain is depicted by the small box in Fig. 3a). Bands with a wavelength of ~180 km in the TKE and Richardson number fields are directly associated with these features in both the horizontal plane (Fig. 3c) and in a vertical cross section taken from the 3-km resolution version of the CH model in a direction perpendicular to the bands and the general flow direction (Fig. 3d). Bands of wave-induced Ri < 1 (associated with sub-grid turbulence) in this vertical plane are evident above 10 km. Lane et al. (2004) shows that these bands were the result of gravity wave modulation of the background shear and stability fields, which reduced the Richardson number within the low static stability phase regions of the gravity-inertia waves, resulting in parallel bands of reduced Ri (thus, increased TKE). Therefore, the regions of (parameterized) turbulence are directly related to the gravity waves despite the fact that the CH model did not directly simulate significant turbulence at the resolvable scales of motion; rather, TKE arose entirely from the sub-grid parameterization scheme.

Koch et al. (2005) show that the gravity waves in the RUC model were triggered in a region of highly unbalanced flow very near to the G-IV path. Imbalance was diagnosed as the residual of the nonlinear balance equation. The imbalance occurred in the vicinity of the tropopause fold, similar to the idealized modeling studies of Reeder and Griffiths (1996) and Zhang (2004), but the imbalance was actually maximized where the secondary tropopause fold joined with the primary fold (near the intersection of the 300-hPa level with the rightmost vertical line in Fig. 2b). The existence of the gravity waves directly above the secondary tropopause fold and immediately downstream of the region of strong upper-level frontogenesis thus appears to have been more than just a coincidence.

Additional examination revealed strong confluence in the alongstream ageostrophic flow in the vicinity of the upper-level front. This created an environment favorable for ageostrophically forced alongstream frontogenesis. The resultant along-jet cold advection in the presence of cyclonic horizontal shear shifted the thermally direct ageostrophic circulation in the jet entrance region toward the anticyclonic side of the jet axis. Consequently, the region of maximum subsidence became located beneath the jet axis (not shown) – a pattern that is highly frontogenetical with respect to the vorticity field (Keyser and Shapiro 1986). This positive feedback loop between frontogenesis and increasing subsidence along the jet axis is a process that is conducive to tropopause folding and unbalanced frontogenesis, and thus, to the generation of gravity-inertia waves.

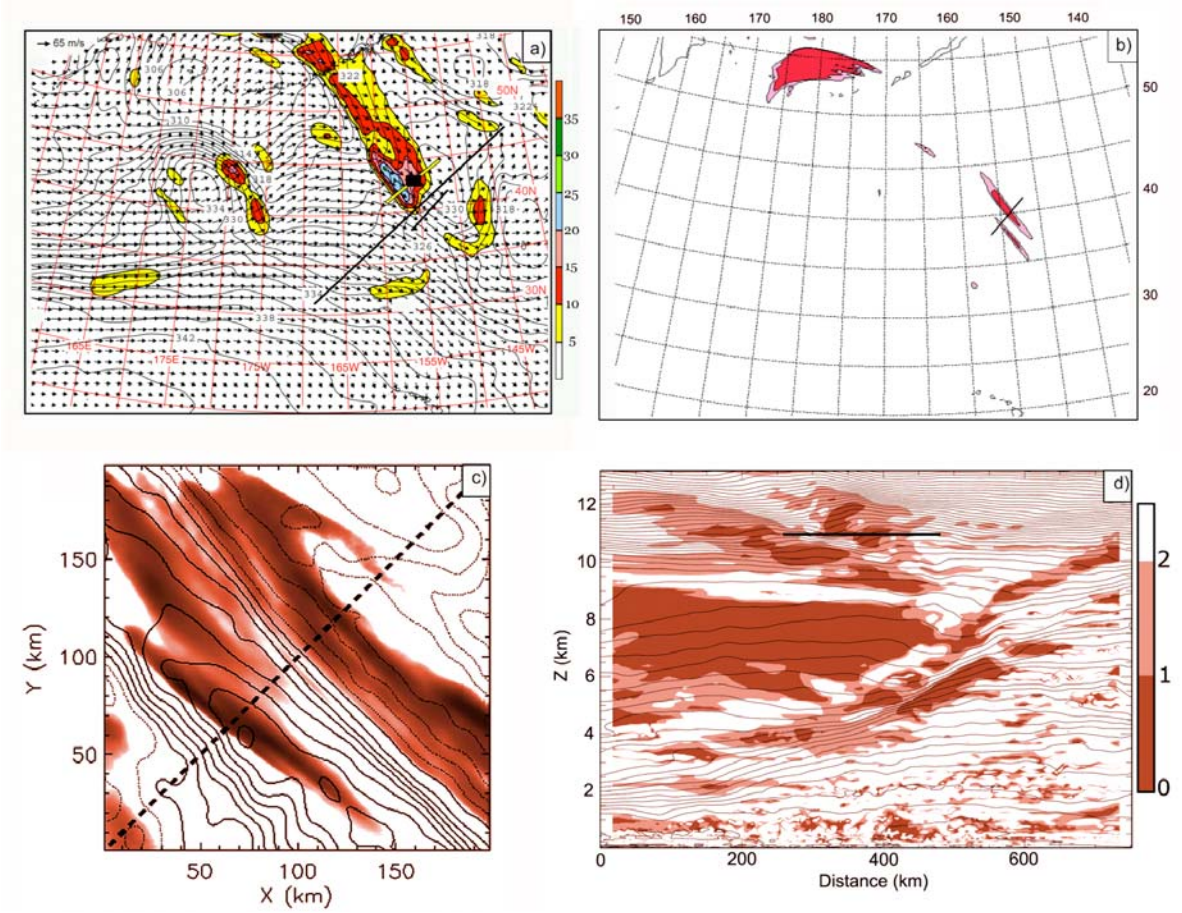

Fig. 3. (a) Virtual potential temperature (2^0C isotherms, black contours), frontogenesis function (color shading, intervals of 5^oK (100 km)$^{-1}$ (3h)$^{-1}$) and wind vectors at 275 hPa from RUC analysis at 0000 UTC 18 Feb; (b) DTF3 at 10.1 km from 6-h RUC forecast valid at 0300 UTC, (c) sub-grid TKE and perturbation potential temperature (0.5 K interval, solid = positive, dotted = negative) at 11 km MSL at 0600 UTC from CH 1-km domain model shown by the small black box in (a), and (d) cross section of Richardson Number and potential temperature (2K intervals) fields from CH model along the southwest-northeast diagonal through the small black box. Black lines in (a) denote locations of RUC cross-sections (long segment) and NE-SW part of the G-IV track (short segment); yellow line through the small black box depicts location of CH model cross section shown in (d). Horizontal line in (d) depicts location of 11-km altitude plot in (c). Light pink and red shading in (b) represents DTF3 ≥3.0 and 4.0 m^2 s^{-2}, corresponding to moderate and severe levels of turbulence, respectively. The red shading in (c) is linear with the maximum value of 0.2 m^2 s^{-2} denoted by the darkest shade.

4. SPECTRAL AND WAVELET ANALYSES OF THE AIRCRAFT DATA

Autospectral analyses of the 25-Hz aircraft data were conducted to determine the dominant frequencies and wavelengths of the gravity waves and their relationship to turbulence. Cross-spectral analyses provided an understanding of the phase relationships between variables needed for proper determination of which spectral signals were manifestations of gravity waves and which represented turbulence. Wavelet analyses were performed to overcome the natural limitations imposed by the "global" nature of spectrum analysis. The spectral energy transfer process was investigated using third-order structure functions.

The power spectra of the vertical acceleration data for 0030–0042 UTC (when there was an absence of significant turbulence) was markedly different than those for 0043–0050 UTC (when one of the strongest and most persistent turbulence events occurred). A strong peak appeared in spectra for both intervals of time at f = 0.06 (Koch et al. 2005). This corresponds to a spatial wavelength of 3.8 km, which is representative of the shorter end of the gravity wave spectrum for this case. However, a peak at 0.65 Hz (corresponding to a wavelength of 350 m) appeared only during the turbulent episode. This peak falls at the lower frequency end of the $k^{-5/3}$ spectral slope region defining the "inertial subrange" (Gage 1979; Lilly 1983; Nastrom and Gage 1985; Cho and Lindborg 2001). The cross-spectral analyses showed high coherence along with a strong "in-phase covariance" in the phase spectrum (consistent with the polarization relation for internal gravity waves) for wavelengths of 0.7–20 km at all four flight levels. Phase angles for potential temperature and longitudinal velocity were highly concentrated near 0^0 or 180^0, a result that is consistent with the polarization equation for gravity waves.

Spectral approaches enable separation of waves from turbulence, but they are valid only in a "global" sense, because a sufficiently long record characterized by "statistical stationarity" is required. Since spectral analysis can only provide such nonlocal information, and does not work well for small-amplitude waves, waves of short duration, and non-monochromatic waves, it is not well suited to the study of intermittent, nonstationary phenomena such as turbulence, which displays rapid changes in phase, amplitude, and statistical properties. The wavelet transform coefficients provide information about both the amplitude and phase of the fluctuations at each time and frequency, and therefore, should be able to provide understanding of the evolving relationship between wave and turbulence characteristics. We applied continuous wavelet analysis to the horizontal wind, temperature, and vertical acceleration data obtained from the G-IV. For the transformation kernel function in the wavelet analysis, we used the continuous Morlet wavelet.

Wavelet results from the 0031–0051 UTC interval (Fig. 4a) show the sporadic appearance of multiple modes during this interval. This wavelet analysis supports the prediction from linear theory that the amplitude of the turbulence should be correlated with the amplitude of the progenitor gravity waves, such that the turbulence intensity oscillates with the wave period. The wavelet results were used to reconstruct the gravity waves in the f = 0.06–0.09 Hz band (wavelengths of 3.8–7.7 km). Comparison of the resulting analysis (Fig. 4c) to the time series of turbulent intensity in the 0.3–0.9 Hz band (wavelengths of 0.2–0.8 km) shown in Fig. 4d reveals that the times of occurrence of the strongest gravity wave amplitudes and the appearance of episodes of high turbulence energy were highly correlated. This behavior is particularly impressive during the extensive 0103–0110 UTC turbulence/wave episode (which extended for nearly 100 km). Closer inspection reveals that the higher-frequency gravity waves tended to occur in packets defined by wave envelopes of various sizes ranging from 7–20 km (Fig. 4e). Turbulence intensity most strongly correlated with these wave packets. The mechanism for turbulence production in these data is believed to be related to non-linear advection, which causes the wave front to become steeper with increasing amplitude until it breaks, resulting in energy transport to turbulence (Weinstock 1986, 1987).

5. STRUCTURE FUNCTION, CROSS-SPECTRAL WAVELET, AND STOKES PARAMETER ANALYSES

Neither the power spectrum nor the wavelet approach can resolve the longstanding controversy about the nature of the kinetic energy cascade in the scales from the mesoscale to the inertial subrange, where the spectrum takes the form described by Kolmogorov (1941):

$$E = C_k \varepsilon^{\frac{2}{3}} k^{-\frac{5}{3}}.$$

Here k is the horizontal wavenumber, C_k is the Kolmogorov constant, and ε is the energy dissipation rate. However, the sign of the third-order structure function can be used to determine the direction of the energy cascade. In the inertial subrange, the third-order diagonal structure function for the difference in the horizontal velocity between two points separated by distance r along the flight track is

$$\left\langle \left(\delta u_L\right)^3 \right\rangle + 2\left\langle \delta u_L \left(\delta u_T\right)^2 \right\rangle = -\frac{4}{3}\varepsilon r$$

The angle brackets denote ensemble averaging, and u_L and u_T are the longitudinal and transverse components, respectively (Cho et al. 2001). The energy cascade is directed from large to small scales if the above expression is negative, and in the opposite direction if positive (Frisch 1995; Lindborg 1999; Cho and Lindborg 2001).

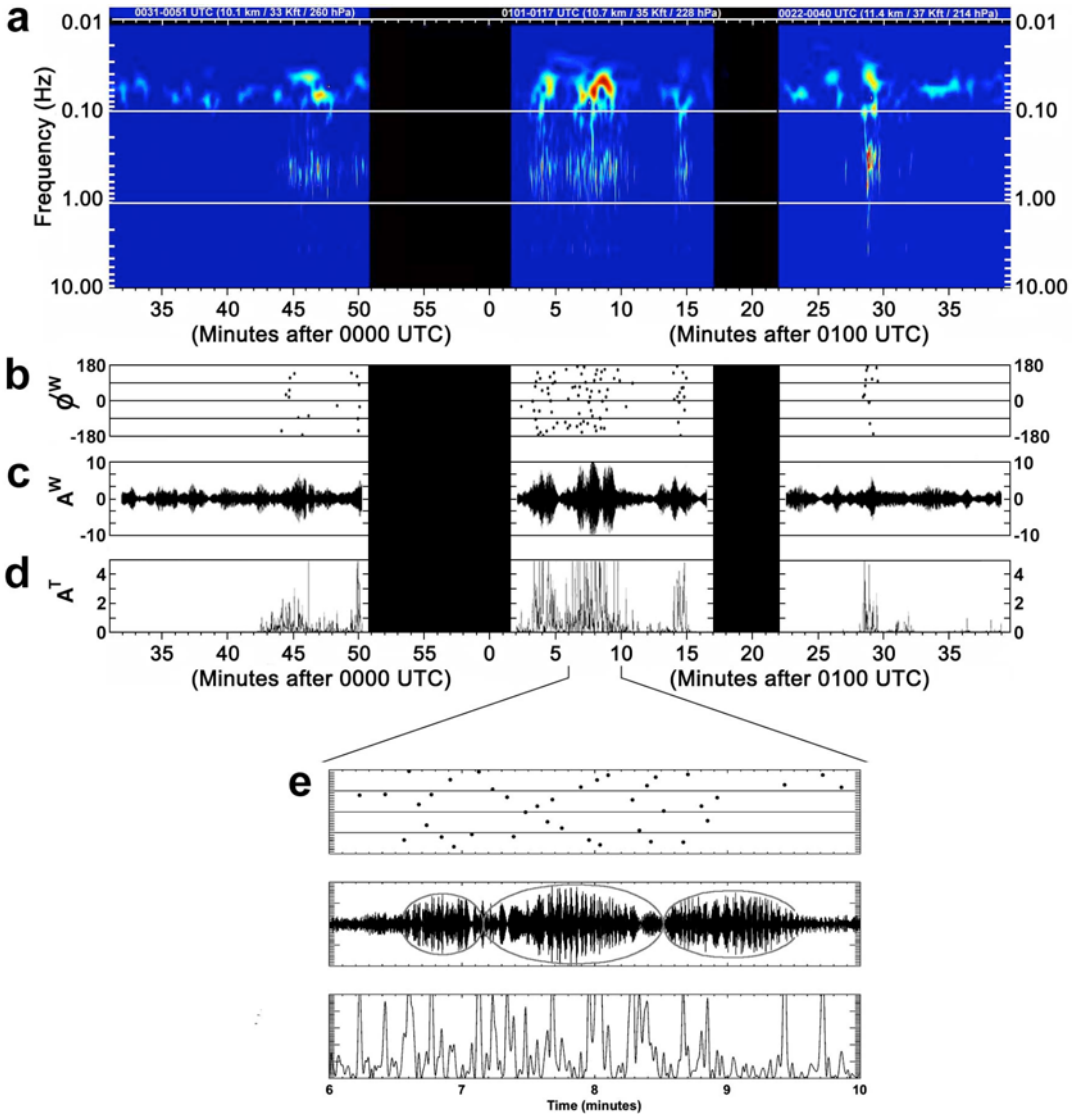

Fig. 4. Wavelet analysis of aircraft vertical acceleration data: (a) time-frequency display of wavelet amplitude at 10.1, 10.7, and 11.4 km; (b) phase ϕ^W of gravity waves (degrees) at which maximum turbulence intensity occurred (only if larger than 0.5 $m^2 s^{-4}$); (c) amplitude A^W ($m s^{-2}$) of gravity waves reconstructed from wavelet analysis for the 0.06–0.09 Hz frequency band; (d) turbulence intensity A^T ($m^2 s^{-4}$) at a frequency of 0.65 Hz; (e) zoomed-in display of panels b, c, d for the period 0106–0110 UTC showing three wave packets (envelopes) by the ellipses. Background noise level of wavelet amplitudes is depicted in blue in panel a, with increasing intensity shown in yellow and red shading (contributions at frequencies greater than 1 Hz have been filtered out of this display). Black segments indicate times when the aircraft was going through maneuvers (primarily changes in altitude) that invalidated the measurements.

The resulting third-order diagonal structure function (Fig. 5) shows a negative *r* dependence for separation distances between 10 and 300m, a positive *r* dependence in the range from 300 to 700m, and a negative r^2 dependence at scales > 700m. These results are consistent with the Kolmogorov theory applicable to the structure function in the inertial subrange and with Cho and Lindborg (2001). The structure function analysis provides strong support for our contention that instabilities created by gravity waves at scales of ~1 – 100 km created conditions conducive to the generation of turbulence (rather than that the waves and turbulence were spontaneously generated at the same time). An intriguing result from this analysis is that a convergence of energy transfer from two directions occurred at a scale of ~700m: from phenomena at scales of 300 – 700 m and from the gravity waves with scales larger than 1 km. Since phenomena at this scale of ~700m would likely develop most rapidly, these results suggest that turbulence was most strongly forced at this scale.

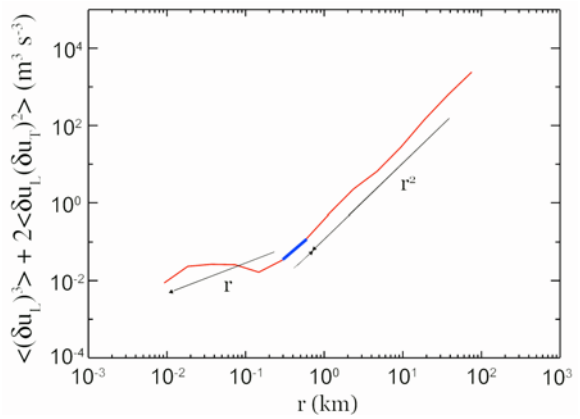

Fig. 5. Diagonal third-order structure functions for the sum of the longitudinal and transverse horizontal velocity components obtained from the 25-Hz G-IV aircraft data at the 10.1-km flight level. Red denotes negative sign indicative of downscale energy transfer. Blue denotes positive sign indicative of upscale energy transfer. Arrows indicate sense of energy transfer and slope of lines. Convergence of energy transfer occurs at a separation distance of ~700 m.

The task of separating gravity waves from stochastic turbulence is made easier by recognizing that for internal gravity waves, the two components of the horizontal perturbation velocity have a linear polarization with a phase angle of $\varphi = n\pi$ (n = 0, ±1). This is in contrast to inertia-gravity waves, which possess an elliptic polarization with a phase angle of $\varphi = n\pi/2$. We used this fact from linear wave theory to distinguish internal gravity waves from turbulence in cross-spectral analyses of the aircraft data. The resulting coherency and phase angle results for the two wind components (Fig. 6) show three statistically significant spectral peaks with a phase angle of almost exactly ±180° at frequencies of 0.012, 0.045, and 0.061 Hz (horizontal wavelengths of 19, 5.1, and 3.7 km). Lu et al. (2005a) performed wavelet transformations on each of these wave modes identified in the cross spectra in order to study the temporally (spatially) varying properties of the waves. This is distinct from Fourier decomposition, which only retrieves a time-invariant wave harmonic over a selected time interval. An example is shown in Fig. 7 for the reconstructed u-wind, v-wind, and potential temperature perturbations for the 0.061 Hz wave. In this case, as well as the other two monochromatic waves, localized wave envelope structures are apparent, with durations of 1–2 min (15–30 km distance). This result is consistent with the frequency band-averaged finding in the vertical acceleration data (Fig. 4).

The final step in our analysis methodology is to introduce the results from the cross-spectral wavelet analysis into the Stokes parameter analysis for partially polarized internal waves. Cho et al. (1999) showed that by applying the Stokes parameter methodology, the polarization relationship between the zonal and meridional components of the horizontal perturbation wind is a good indication of the presence of gravity waves vs. turbulence. Earlier, Vincent and Fritts (1987) and Eckermann and Vincent (1989) had used the Stokes technique to study upper-atmospheric gravity-inertia waves, but not turbulence.

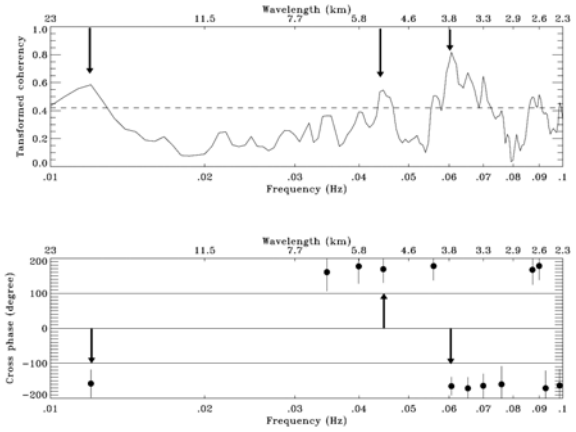

Fig. 6. Cross spectra for the zonal and meridional velocities: a) transformed coherency, and b) the phase angle. Peaks of the coherency spectrum above the dashed line are 95% statistically significant, and the error-bars in the phase diagram represent 95% confidence intervals for the computed phase difference (at the center of each circle). Arrows emphasize significant peaks discussed in the text.

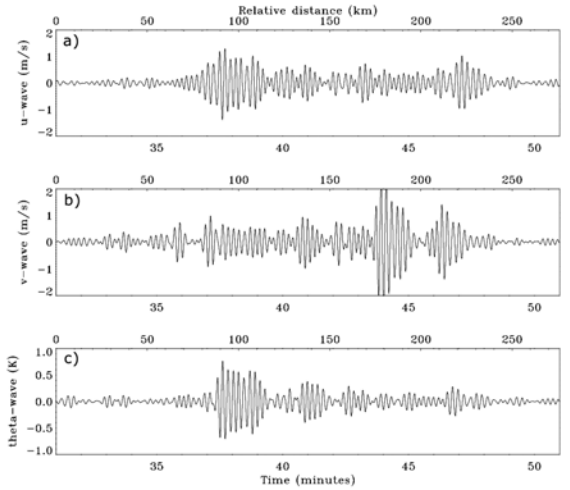

Fig. 7. Reconstructed monochromatic gravity wave of frequency = 0.061 Hz for a) u-wind ; b) v-wind; and c) potential temperature θ.

Customary Stokes parameter analysis uses time averaging of the squared wave-amplitudes of the two components of the wind. Problems exist when one attempts to properly choose the data window for performing time averaging under the assumption of statistical invariance of the wave properties

throughout the selected data segments (a problem shared with traditional spectral analysis). For this reason, we developed a frequency averaging method (Lu et al. 2005b): by identifying a transitional frequency, a division of the full spectrum into gravity wave and turbulence sub-spectra can be obtained; accordingly, one can localize the spatial and temporal variability of polarizations for gravity waves, while for turbulence the polarization may not be definable. The four Stokes parameters are:

- The degree of polarization, which measures the ratio of completely polarized power to the total power
- The major axis orientation of the polarization ellipse, which predicts the direction of the horizontal component of the wave vector
- The coherency, which measures the correlated power between the two wind components
- The phase angle between the two wind components as a function of frequency, which measure which type of polarization is dominant (e.g., $\varphi = n\pi$ for linear).

Plots of these four parameters, as well as the turbulence intensity, as a function of time for the frequency-averaged band f = 0.01–0.20 Hz are shown in Fig. 8. The shaded regions correspond to the periods when turbulence occurrence was identified by (1) visual inspection of the time series of the wind components, which displayed an abrupt increase in variance at 0043 UTC, which is when the pilot first reported encountering moderate turbulence, and also from (2) when the wavelet analysis shows the sudden appearance of the high-frequency turbulence signal (Fig. 4d). These measures of "turbulent episodes" agree well with the turbulence intensity computed from the spectra of the high-frequency band (Fig. 8e).

It can be seen that the degree of polarization and the coherency display strikingly similar patterns (Fig. 8a and 8c), and that gravity waves show an enhanced level of polarization (>60%) and coherency (>0.6) at those times when the turbulence began to occur. Also, note the increased numbers of sharp peaks in these two Stokes parameters during the diagnosed turbulence time periods (especially 0043–0049 UTC). This suggests the hypothesis that turbulence generation instantaneously reduces the gravity wave polarization simultaneously with the loss of wave energy. Finally, note that the phase angles (Fig. 8d) between the two horizontal wind components vary approximately as ±180°, suggestive of a spectrum of small-scale internal gravity waves displaying linear polarization.

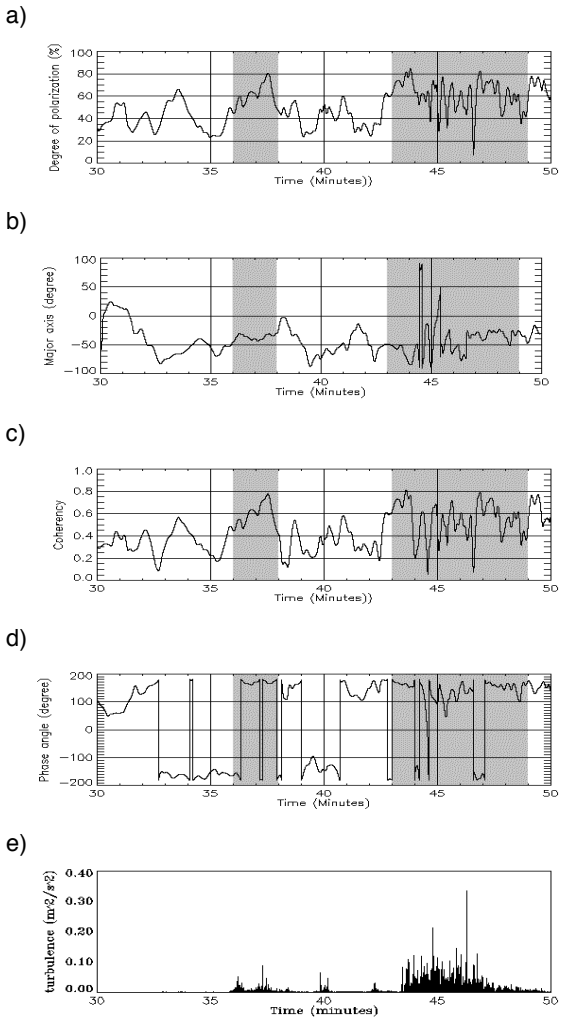

Fig. 8. Localization of the Stokes parameters in the time domain for the gravity-wave spectrum (f = 0.01–0.2 Hz): a) degree of polarization; b) orientation of the major axis; c) coherency; and d) phase angle. The bottom plot (e) shows the temporal variation of turbulence intensity. The shaded regions indicate the time periods when turbulence was detected (see text).

6. CONCLUSIONS

High-resolution aircraft measurements and simulations from numerical models are analyzed for a clear-air turbulence event associated with an intense upper-level jet/frontal system. Cross spectral, wavelet, structure function and Stokes parameter analyses performed with the 25-Hz in-situ aircraft data are used to investigate the relationship between gravity waves and turbulence. Mesoscale dynamics are analyzed with the 20-km hydrostatic Rapid Update Cycle (RUC) model, and a nested 1-km simulation with the nonhydrostatic Clark-Hall (CH) model.

Inertia-gravity waves were generated within a region of unbalanced frontogenesis in the vicinity of a complex tropopause fold above the jet core. Turbulent Kinetic Energy fields forecast by the models displayed a strongly banded appearance associated with these mesoscale gravity waves. Smaller-scale gravity wave packets (wavelengths of 1–20 km) within the mesoscale wave field perturbed the background wind shear and stability, promoting the development of bands of reduced Richardson number conducive to the generation of turbulence.

The wavelet analysis revealed that brief episodes of high turbulent energy were closely associated with gravity wave occurrences. Structure function analysis provided evidence that turbulence was most strongly forced at a horizontal scale of 700 m. By combining cross-spectral and continuous wavelet transformation, we were able to extract the temporal and spatial characteristics of the waves. Upon further introduction of these results into a Stokes parameter analysis for partially polarized internal waves, we demonstrated that gravity waves possess distinctive polarization and coherency signatures allowing clear separation of waves from turbulence. Our analysis indicates that the turbulence production is closely related to an enhancement in both the polarization and coherency above a threshold value in the Cartesian wind components, and that turbulent surges are accompanied by an abrupt reduction of the polarization and shifting of the horizontal wave vector. The implications of this research are that unbalanced upper-level jets may generate a broad spectrum of gravity waves, which at the shorter wavelengths, develop a tendency to steepen and break, resulting in surges of turbulent bursts that are readily identifiable using spectral, wavelet, and structure function techniques.

7. ACKNOWLEDGMENTS

Contributors to this multi-part investigation appear in the published papers by Koch et al. (2005), Lu et al. (2005 a, b), and Lane et al. (2004), in particular Brian Jamison, Tracy Smith, Ning Wang, and Ed Tollerud, all from NOAA/ESRL, and Todd Lane from NCAR. The authors express their appreciation to Chris Webster at NCAR for assistance with the spectral analysis, to Jack Parrish at the NOAA Aircraft Operations Center for guidance in the proper use of the aircraft data, and to Fernando Caracena for the analysis of unbalanced flow.

8. REFERENCES

Benjamin, S. G., G. A. Grell, J. M. Brown, and T. G. Smirnova, 2004a: Mesoscale weather prediction with the RUC hybrid isentropic–terrain-following coordinate model. *Mon. Wea. Rev.,* **132,** 473–494.

Benjamin, S. G., D. Dévényi, S. S. Weygandt, K. J. Brundage, J. M. Brown, G. A. Grell, D. Kim, B. E. Schwartz, T. G. Smirnova, and T. L. Smith, 2004b: An Hourly Assimilation–Forecast Cycle: The RUC. *Mon. Wea. Rev.,* **132,** 495–518.

Cho, J. Y. N., and E. Lindborg, 2001: Horizontal velocity structure functions in the upper troposphere and lower stratosphere. 1. Observations. *J. Geophys. Res.,* **106,** (10), 223–232.

Cho, J. Y. N., B. E. Anderson, J. D. W. Barrick, and K. L. Thornhill, 2001: Aircraft observations of boundary layer turbulence: Intermittency and the cascade of energy and passive scalar variance. *J. Geophys., Res.,* **106,** 32 469 – 32 479.

Cho, J. Y. N., R. E. Newell, and J. D. Barrick, 1999: Horizontal wavenumber spectra of winds, temperature, and trace gases during the Pacific Exploratory Missions: 2. Gravity waves, quasi-two-dimensional turbulence, and vertical modes. *J. Geophys. Res.*, **104,** 16,297-16,308.

Clark, T. L., 1977: A small-scale dynamic model using a terrain-following coordinate transformation. *J. Comp. Phys.,* **24,** 186–215.

Clark, T. L., W. D. Hall, R. M. Kerr, D. Middleton, L. Radke, F. M. Ralph, P. J. Neiman, and D. Levinson, 2000: Origins of aircraft-damaging clear-air turbulence during the 9 December 1992 Colorado downslope windstorm: Numerical simulations and comparison with observations. *J. Atmos. Sci.,* **57,** 1105–1131.

Cot, C., and J. Barat, 1986: Wave-turbulence interaction in the stratosphere: A case study. *J. Geophys. Res.,* **91,** (D2), 2749–2756.

Demoz, B. B., D. O'C. Starr, K. R. Chan, and S. W. Bowen, 1998: Wavelet analysis of dynamical processes in cirrus. *Geophys. Res. Lett.*, **25,** 1347–1350.

Eckermann, S. D., and A. Vincent, 1989: Falling sphere observations of anisotropic gravity wave motions in the upper stratosphere over Australia. *Pure Appl. Geophys.*, **130,** 509-532.

Frisch, U., 1995: *Turbulence: The Legacy of A. N. Kolmogorov*, 296 pp., Cambridge Univ. Press, New York.

Gage, K.S., 1979: Evidence for a $k^{-5/3}$ power law inertial range in mesoscale two-dimensional turbulence. *J. Atmos. Sci.,* **36,** 1950–1954.

Gultepe, I., and D. O'C. Starr, 1995: Dynamical structure and turbulence in cirrus clouds: aircraft observations during FIRE. *J. Atmos. Sci*., **52,** 4159–4182.

Hines, C. O., 1963: The upper atmosphere in motion. *Quart. J. Roy. Meteor. Soc*., **89,** 1–42.

Hodges, R. R., 1967: Generation of turbulence in the upper atmosphere by internal gravity waves. *J. Geophys. Res*., **72,** 3455–3458.

Hodur, R. M., 1997: The Naval Research Laboratory's Coupled Ocean/Atmosphere Mesoscale Prediction System (COAMPS). *Mon. Wea. Rev.,* **125,** 1414–1430.

Keyser, D., and M. A. Shapiro, 1986: A review of the structure and dynamics of upper–level frontal zones. *Mon. Wea. Rev.,* **114,** 452–499.

Koch, S. E., B. D. Jamison, C. Lu, T. L. Smith, E. I. Tollerud, C. Girz, N. Wang, T. P. Lane, M. A. Shapiro, D. D. Parrish, and O. R. Cooper, 2005: Turbulence and gravity waves within an upper-level front. *J. Atmos. Sci.,* **62,** 3885–3908.

Koch, S. E., and F. Caracena, 2002: Predicting clear-air turbulence from diagnosis of unbalanced flow. Preprints, *10th Conf. on Aviation, Range, and Aerospace Meteorology*, Portland, OR, Amer. Meteor. Soc., 359–363.

Kolmogorov, A. N., 1941: The local structure of turbulence in compressible viscous fluid for very large Reynolds number. *Dokl. Akad. Nauk SSSR*, **30,** 299 – 303.

Lane, T. P., J. D. Doyle, R. Plougonven, M. A. Shapiro, and R. D. Sharman, 2004: Observations and numerical simulations of inertia-gravity waves and shearing instabilities in the vicinity of a jet stream. *J. Atmos. Sci*., **61,** 2692–2706.

Lilly, D. K., 1983: Stratified turbulence and the mesoscale variability of the atmosphere. *J. Atmos. Sci*., **40,** 749–761.

Lindborg, E., 1999: Can the atmospheric kinetic energy spectrum be explained by two-dimensional turbulence? *J. Fluid Mech*., **388,** 259 – 288.

Lindzen, R. S., 1987: Supersaturation of vertically propagating internal gravity waves. *J. Atmos. Sci*., **45,** 705–711.

Lu, C., S. Koch, and N. Wang, 2005a: Determination of temporal and spatial characteristics of atmospheric gravity waves combining cross-spectral analysis and wavelet transformation. *J. Geophys. Res*., **110,** *D01109, doi:10.1029/2004JD004906*.

Lu, C., S. Koch, and N. Wang, 2005b: Stokes parameter analysis of turbulence-generating gravity waves combining cross-spectral analysis and wavelet transformation. *J. Geophys. Res.,* **110,** doi:10.1029/2004JD005736.

Morlet, J., G. Arens, E. Fourgau, and D. Giard, 1982: Wave propagation and sampling theory – Part I: Complex signal and scattering in multilayered media. *Geophys*., **47,** 203–221.

Nastrom, G. D., and K. S. Gage, 1985: A climatology of atmospheric wavenumber spectra of wind and temperature observed by commercial aircraft. *J. Atmos. Sci*., **42,** 950–960.

Reeder, M. J., and M. Griffiths, 1996: Stratospheric inertia-gravity waves generated in a numerical model of frontogenesis. I: Wave sources, generation mechanisms and momentum fluxes. *Quart. J. Roy. Met. Soc.,* **122,** 1175–1195.

Shapiro, M. A., 1978: Further evidence of the mesoscale and turbulence structure of upper level jet stream-frontal zone systems. *Mon. Wea. Rev*., **106,** 1100–1111.

Uccellini, L. W., and S. E. Koch, 1987: The synoptic setting and possible source mechanisms for mesoscale gravity wave events. *Mon. Wea. Rev.,* **115,** 721–729.

Vincent, R. A., and D. C. Fritts, 1987: A climatology of gravity wave motions in the mesopause region at Adelaide, Australia. *J. Atmos. Sci*., **44,** 748-760.

Weinstock, J., 1986: Finite amplitude gravity waves: Harmonics, advective steepening and saturation. *J. Atmos. Sci.,* **43,** 688–704.

Weinstock, J., 1987: The turbulence field generated by a linear gravity wave. *J. Atmos. Sci.,* **44,** 410–420.

Zhang, F., 2004: Generation of mesoscale gravity waves in upper-tropospheric jet-front systems. *J. Atmos. Sci.,* **61,** 440–457.